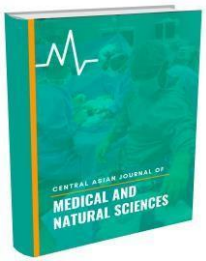

CENTRAL ASIAN JOURNAL OF MEDICAL AND NATURAL SCIENCES
https://cajmns.centralasianstudies.org/index.php/CAJMNS
Volume: 07 Issue: 02 | April 2026 ISSN: 2660-4159

.

Article

Study of a Surface Plasmon Resonance-Based Optical Fiber Sensor for Nitrate Detection

Mohammed Hussein Ibrahim*[1], Rasoul Aalipour Kosalar[2]

1,2. Department of Physics, College of Education for pure Science, University of Azarbaijan Shahid Madani
* Correspondence: aljbory729@gmail.com

Abstract: This article presents the design, simulation, and analysis of a surface plasmon resonance (SPR) sensor based on solid twin-core photonic crystal fibers (PCFs) for detecting nitrate concentration in aqueous solutions. The motivation stems from the urgent need for sensitive, compact, real-time monitoring systems capable of addressing the growing challenges of water pollution and environmental management. The sensor structure was designed and simulated using COMSOL Multiphysics, with gold as the plasmonic layer and aqueous nitrate solutions as the analyte. The study investigated the variation of the effective refractive index and confinement loss with wavelength in the range of 800–1800 nm, complemented by two-dimensional field distributions to visualize plasmon coupling at the fiber-metal-analyte interface. The results showed that the resonance wavelength shifts to red in a consistent manner with increasing nitrate concentration, confirming the strong dependence of the plasmonic phase matching on the refractive index of the material to be analyzed. The sensitivity of the sensor was evaluated from the slope of the linear fit of the Re(n_eff) data versus wavelength, expressed in RIU/nm, and the derived values showed an approximately linear increase across the studied concentration range, confirming the validity of the proposed scale. Overall, the results confirm that the proposed dual-core PCF–SPR sensor offers high sensitivity, predictable performance, and practical potential for monitoring nitrates in water, providing a basis for future experimental investigation and application in the field of environmental sensing.

Keywords: Photonic Crystal Fiber, Surface Plasmon Resonance, Nitrate, Optical Sensitivity

Citation: Ibrahim, M. H., Kosalar, R. A. Study of a Surface Plasmon Resonance-Based Optical Fiber Sensor for Nitrate Detection. Central Asian Journal of Medical and Natural Science 2026, 7(2), 16-29.

Received: 30th Dec 2025
Revised: 15th Jan 2026
Accepted: 30th Jan 2026
Published: 12th Feb 2026

1. Introduction

The rapid advancement of optical technologies has significantly transformed sensing applications across scientific and industrial fields [1]. Environmental monitoring, in particular, has emerged as one of the most critical areas where advanced sensing is urgently required. Among the various environmental concerns, water quality has become a global priority, as billions of people still lack access to safe drinking water [2]. Agricultural fertilizers, industrial discharges, and food processing practices have led to widespread contamination of water resources with nitrate compounds [3]. These pollutants, when present in high concentrations, negatively impact aquatic ecosystems and pose serious health threats to humans. Infants, in particular, are vulnerable to nitrate contamination, which can cause methemoglobinemia or "blue baby syndrome," a life-threatening condition that impairs oxygen transport in the blood.[4][5][6] Conventional techniques for nitrate detection, such as chromatography, electrochemical sensors, and spectroscopic methods, have been widely used in laboratory settings. While accurate, these

methods often involve expensive instruments, skilled personnel, and long detection times, limiting their suitability for real-time and field applications. This challenge has encouraged researchers to explore optical fiber sensors, which offer distinct advantages such as compactness, immunity to electromagnetic interference, remote sensing capability, and cost-effectiveness [7][8][9] Among optical fibers, photonic crystal fibers (PCFs) have gained increasing attention due to their microstructured cladding composed of periodic arrays of air holes [10]. Unlike conventional fibers, PCFs can manipulate light propagation in highly controllable ways, leading to enhanced light–matter interactions. By leveraging these properties, PCFs have shown remarkable potential for chemical and biochemical sensing applications [11] , Surface Plasmon resonance (SPR) is one of the most effective mechanisms for enhancing PCF-based sensing. SPR arises when incident light couples with collective oscillations of free electrons at the interface of a plasmonic material and a dielectric[12][13]. This phenomenon is highly sensitive to changes in the refractive index of the surrounding medium [14]. The integration of SPR with PCFs allows for the development of sensors that are compact, tunable, and capable of detecting extremely small variations in analyte concentration. When applied to nitrate detection in water, PCF-SPR sensors can achieve rapid, reliable, and cost-effective measurement [15][16][17].

2. Computational Details

The methodology adopted in this research integrates the theoretical foundations of surface Plasmon resonance (SPR) sensing, the distinctive properties of photonic crystal fibers (PCFs), and the computational modeling capabilities of COMSOL Multiphysics to design and evaluate a solid dual-core PCF-based SPR sensor for nitrate detection. This chapter begins by introducing the underlying principles and strengths of SPR as a highly sensitive optical phenomenon for chemical and biological sensing. It then outlines the unique structural and functional attributes of PCFs that make them excellent platforms for integrated plasmonic sensors. Finally, the role of COMSOL Multiphysics in enabling accurate numerical modeling, simulation, and optimization of such devices is emphasized. Collectively, these foundations establish the framework for the design strategy presented in subsequent sections. SPR is one of the most widely investigated optical sensing mechanisms because of its ability to detect minute changes in the refractive index of a medium adjacent to a metallic interface. The phenomenon arises when incident light couples to free electron oscillations at the boundary between a dielectric material and a thin metallic layer, such as gold or silver. This coupling leads to the generation of surface Plasmon Polaritons (SPPs), which are highly sensitive to environmental variations, particularly changes in the local refractive index. When the refractive index of the analyte medium shifts, the resonance condition is altered, resulting in a measurable change in parameters such as resonance wavelength, angle, or intensity. The sensitivity and selectivity of SPR-based sensors make them particularly suitable for detecting low concentrations of chemical and biological targets in aqueous environments. Nitrate detection is a pressing application due to the environmental and health concerns associated with nitrate contamination in natural water bodies. Traditional detection techniques, while accurate, often require complex laboratory instrumentation and time-consuming sample preparation. In contrast, SPR-based sensors offer label-free, real-time monitoring with high precision, making them a compelling alternative. Additionally, by integrating SPR with engineered photonic structures, such as PCFs, both sensitivity and design flexibility can be significantly enhanced. Photonic crystal fibers (PCFs) represent a new generation of optical waveguides distinguished by their periodic microstructured arrangement of air holes running along the fiber length. This unique architecture provides far greater control over light propagation than conventional fibers, enabling features such as endlessly single-mode operation, tunable dispersion, and enhanced nonlinear effects. Depending on their design, PCFs can guide light either through modified total internal

reflection (index-guiding PCFs) or through the photonic bandgap effect (hollow-core PCFs).

3. Results and Discussion

3.1 COMSOL Multiphysics Implementation

Step 1: Geometry construction

- Draw a solid fiber core (approximate diameter: 6.1 μm).
- Define the cladding with a hexagonal arrangement of circular air holes (cladding diameter ≈ 69 μm, air-hole diameter ≈ 2 μm).
- Utilize COMSOL's Array or Periodic features to replicate the lattice.
- Apply a thin metallic coating (~65 nm Au/Ag) around the cladding exterior by using Offset or Boundary Selection.
- Insert a circular analyte layer (≈ 138 μm in diameter) surrounding the metal.

Step 2: Material properties

- **Core/cladding:** Silica, refractive index ≈ 1.44 at 1550 nm.
- **Metal:** Gold, represented through the Drude-Lorentz dispersion relation [22]:

$$\varepsilon_{\mathrm{Au}} = \varepsilon_{\infty} - \frac{\omega_{\mathrm{p}}^2}{\omega^2 + \mathrm{i}\gamma_{\mathrm{d}}\omega} + \frac{\Delta\varepsilon\,\omega^2}{(\omega^2 - \Omega_{\mathrm{L}}^2) + \mathrm{i}\Gamma_{\mathrm{L}}\omega} \quad (3.1)$$

Here, ε_{Au} is the permittivity of gold, ε_{∞} is the permittivity at high frequency, ω_p and γ_d stand respectively for the plasma frequency and damping coefficient, Ω_L and Γ_L are spectral width and oscillator strength, respectively, and $\Delta\varepsilon$ is the weighting factor.

- Nitrate**:**

Step 3: Physics settings

- Electromagnetic waves, frequency domain (ewfd), within the Wave Optics module.
- Wavelength range defined from $600 - 1800$ nm.
- Outer boundaries equipped with perfectly matched layers (PMLs).
- At the gold–dielectric boundary, SPR is supported when the propagation constant of the guided mode equals that of the plasmonic mode.
- Use Mode Analysis to extract the effective indices of both modes.

Step 4: Meshing

- Generate a refined mesh near the metal and core–cladding interfaces.
- Employ Boundary Layer meshing to accurately capture Plasmon field decay over 20–100 nm into the metal and analyte.

Step 5: Simulation and post-processing

- **Mode analysis:** Compute modal indices of the guided and Plasmon modes to locate resonance wavelengths.
- **Confinement loss:** Determine loss in dB/m from the imaginary part of the modal index [18]:

$$\mathrm{L_c} = 8.686\,\mathrm{k_0}\,\mathrm{Im}[\mathrm{n_{eff}}] \quad (3.2)$$

  Loss peaks correspond to resonance dips, a clear indication of SPR.
- **Field visualization:** Plot electric field intensities at resonance along the gold-dielectric surface.
- **Sensitivity analysis:** Vary the sensing layer index ($\Delta n \approx 0.01 - 0.05\,RIU$) to track SPR wavelength shifts:

$$\mathrm{S\ (nm/RIU)} = \Delta\lambda_{\mathrm{res}} / \Delta\mathrm{n} \quad (3.3)$$

3.2 Design Graphics

Following the methodology in Section 3.3.2, a 2D model of the dual-core PCF was developed. The cladding, composed of a hexagonal arrangement of circular air holes, is overlaid with a thin gold layer.

Table 3.1 summarizes the parameters used in the design, including the radii, refractive indices of core and cladding, air-hole dimensions, operational wavelength, and PML thickness.

For silica's refractive index, the Sellmeier equation was used:

$$n^2 = 1 + \sum_i \frac{B_i \lambda^2}{\lambda^2 - C_i} , \quad (3.4)$$

in which, B_i and C_i are the Sellmeier coefficients [23].

The role of PMLs in COMSOL is to absorb outgoing fields without reflections, ensuring computational stability. The modeled sensor is shown in Figure 3.1.

The optical simulation used the Wave Optics module with Mode Analysis, refined meshing near the core and coating region, and a focus on the resonant wavelength defined in Table 3.1. Figure 3.2 presents the meshing strategy.

Table 1. Parameters of the designed dual-core Au coated-PCF.

Name	Expression	Value	Description
p	1.8[um]	1.8E-6 m	pitch
dc	0.49*p	8.82E-7 m	diameter of core
d1	0.28*p	5.04E-7 m	air hole diameter
d2	0.9*p	1.62E-6 m	air hole diameter
d3	0.97*p	1.746E-6 m	air hole diameter
tau	40[nm]	4E-8 m	thickness of gold layer
ana	p/2	9E-7 m	thickness of analyte
l	0.62[um]	6.2E-7 m	wavelength
A1	0.6961663	0.69617	
A2	0.4079426	0.40794	
A3	0.8974794	0.89748	
B1	4.67914826e-3[um^2]	4.6791E-15 m²	
B2	1.35120631e-2[um^2]	1.3512E-14 m²	
B3	97.9340025[um^2]	9.7934E-11 m²	
neff1	sqrt(1+(A1*l^2)/(l^2-B1)+(A2*l^2)/(l^2-B2)+(A3*l^2)/(l^2-B3))	1.4574	refractive index of silica
einf	5.9673	5.9673	
omg	2*pi*c_const/l	3.0381E15 1/s	
omgD	2*pi*2113.6[THz]	1.328E16 Hz	
lD	2*pi*15.92[THz]	1.0003E14 Hz	
gl	2*pi*104.86[THz]	6.5885E14 Hz	
rl	2*pi*650.07[THz]	4.0845E15 Hz	
De	1.09	1.09	
eg	einf-omgD^2/(omg*(omg+i*lD))-De*rl^2/((omg^2-rl^2)+i*gl*omg)	-10.843+1.2396i	dielectric constant of gold
e1	real(eg)	-10.843	
e2	imag(eg)	1.2396	
nau	sqrt((sqrt(e1^2+e2^2)+e1)/2)	0.18792	refractive index of gold
kau	sqrt((sqrt(e1^2+e2^2)-e1)/2)	3.2982	extinction coefficient of...
na	1.33	1.33	refractive index of analyte

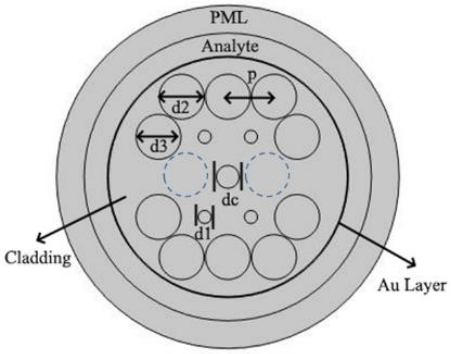

Figure 1. Dual-core Au coated-PCF designing graphics.

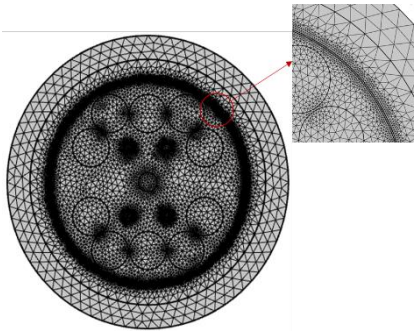

Figure 2. Meshing structure of the proposed sensor for calculating the electric field distribution on the cross of dual-core Au coated-PCF.

The field distribution was obtained for two polarizations of the core mode. As depicted in Figure 3.3, the field remains largely confined to the dual cores. With both TE and TM polarizations present, the field was numerically resolved independent of the thin Au coating. To identify Plasmon resonance, the effective index was scanned between $500 - 750$ nm. The SPR response at 600 nm is illustrated in Figure 3.4.

It is well established that SPR is primarily excited under transverse magnetic (TM) polarization [24]. COMSOL introduces both TE and TM modes, but for TM waves in plasmonic guides:

$$E = (E_x . 0 . E_z) \quad \text{and} \quad H = (0 . H_y . 0) \tag{3.5}$$

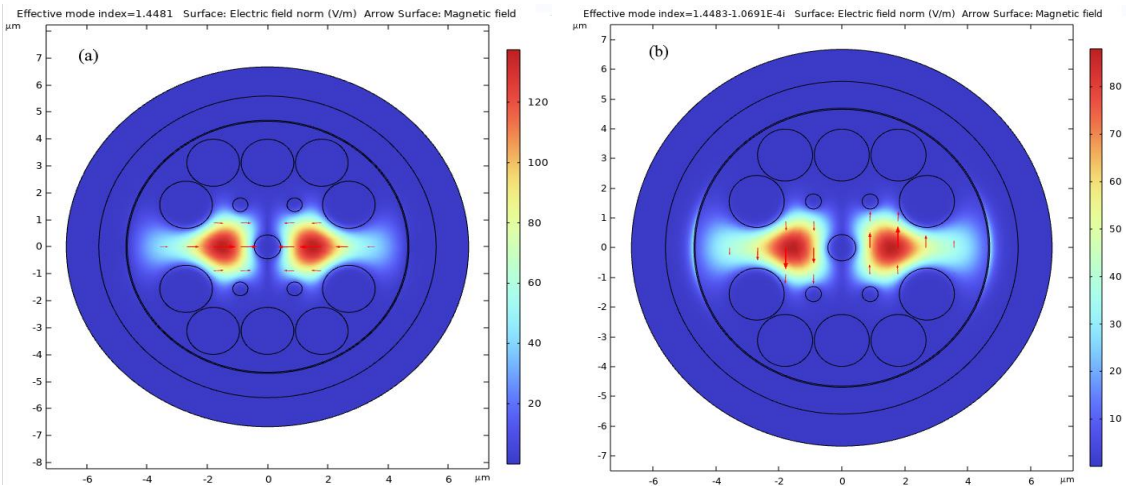

Figure 3. Calculated electric field distribution across the Au coated-PCF for core mode, (a) x-polarization and (b) y-polarization.

3.3 Calculating Effective Refractive Index (n_{eff})

To quantify the effective refractive index of the fundamental guided mode, the following procedure was adopted:

1. Mode analysis setup

- Add Mode Analysis study: Study > Add Study > Mode Analysis.
- Ensure geometry includes core, cladding, metallic coating, and analyte domain.
- Assign materials from Table 3.1.
- Set excitation wavelength (e.g., 800 nm).

2. Computation of n_{eff}

- Run simulation to compute Eigen modes.
- The effective refractive index is obtained as:

$$n_{eff} = \mathrm{Re}(n_{eff}) + i \cdot \mathrm{Im}(n_{eff}) \quad (3.6)$$

$\mathrm{Re}(n_{eff})$: Propagation constant.

$\mathrm{Im}(n_{eff})$: Loss.

3. Parametric wavelength sweep

- Sweep wavelength from $500 - 750$ nm in 10 nm steps.
- Plot $\mathrm{Re}(n_{eff})$ vs. wavelength.
- Compute confinement loss using:

$$L_c = 8.686 \times 2\pi/l \times \mathrm{Im}(n_{eff}) \times 10^4 \ (\mathrm{dB/cm}) \quad (3.7)$$

3.4 Confinement Loss

Confinement loss describes leakage of the guided light from the PCF core into the cladding and surrounding medium. In PCFs, this arises due to the finite number of air-hole rings and their geometric periodicity. Unlike conventional step-index fibers, PCFs rely on engineered air-hole microstructures to confine light.A numerically PCF based SPR biosensor has been proposed and studied. The FEM method has been adopted to model the computational domain of the proposed sensor and a circular perfectly matched layer has been used outside the structure to abolish radiation toward the surface. The proposed sensor shows wavelength sensitivity of 4000 nm/RIU with resolution of 2.5 × 10−5 RIU. Also, the sensor shows the amplitude sensitivity of 265 RIU−1 with resolution of 3.7 × 10−5 RIU. As the sensor is easy to fabricate by using draw and Stack method. Due to promising result and simple sensing scheme we believe that this sensor can be a good candidate for biological and biochemical analyte detection.Through proper optimization, low-loss PCFs can be designed for use in nonlinear optics, communication, and biomedical sensing. Numerical solvers like COMSOL provide a reliable means to balance confinement loss with sensitivity.

3.5 Nitrate Refractive Index in COMSOL Multiphysics

We computed the complex refractive index $\tilde{N}(\lambda) = n(\lambda) + i \cdot k(\lambda)$ for aqueous nitrate solutions over the wavelength range $0.8 - 1.8$ μm (step 0.1 μm) and for concentrations 0%, 10%, 20%, 30%, 40%, 50% (w/w) using a simple, transparent model intended for use as a COMSOL starting dataset. The real part $n(\lambda)$ is built from a baseline refractive index for pure water in the near-IR (assumed to decrease slightly with wavelength from 1.3280 at 0.80 μm to 1.3190 at 1.80 μm) and a linear concentration increment chosen so that a 50% solution raises n by +0.050 (i.e., $\Delta n \approx 0.001$ per % concentration). This linear increment is a pragmatic approximation valid for dilute-to-moderately-concentrated solutions and gives physically plausible refractive indices that scale with concentration. The imaginary part $k(\lambda)$ in the $0.8 - 1.8$ μm region is essentially zero for nitrate (the strong nitrate absorption lies in the deep UV), so k was set to a very small, concentration-scaled value (baseline 1×10^{-8} for pure water, increasing linearly to $\sim 5 \times 10^{-5}$ at 50%) to allow COMSOL to accept a nonzero (but negligible) loss term. Table

3.1 illustrates the real part (n) and imaginary part (k) of the refractive index for aqueous nitrate solutions at concentrations between 0% and 50% (w/w). The values are based on a water baseline dispersion model with a linear concentration increment for n and a small concentration-scaled k to represent negligible absorption in this spectral region. Data are provided in a format suitable for COMSOL simulations.

Table 2. Real part (n) and imaginary part (k) of the refractive index for aqueous nitrate solutions at concentrations between 0% and 50% (w/w), across the near-infrared wavelength range 0.8–1.8 μm in 0.1 μm steps.

λ (μm)	n (0%)	k (0%)	n (10%)	k (10%)	n (20%)	k (20%)	n (30%)	k (30%)	n (40%)	k (40%)	n (50%)	k (50%)
0.8	1.328	1.000E-08	1.338	1.001E-05	1.348	2.001E-05	1.358	3.000E-05	1.368	4.000E-05	1.378	5.000E-05
0.9	1.3271	1.000E-08	1.3371	1.001E-05	1.3471	2.001E-05	1.3571	3.000E-05	1.3671	4.000E-05	1.3771	5.000E-05
1	1.3262	1.000E-08	1.3362	1.001E-05	1.3462	2.001E-05	1.3562	3.000E-05	1.3662	4.000E-05	1.3762	5.000E-05
1.1	1.3253	1.000E-08	1.3353	1.001E-05	1.3453	2.001E-05	1.3553	3.000E-05	1.3653	4.000E-05	1.3753	5.000E-05
1.2	1.3244	1.000E-08	1.3344	1.001E-05	1.3444	2.001E-05	1.3544	3.000E-05	1.3644	4.000E-05	1.3744	5.000E-05
1.3	1.3235	1.000E-08	1.3335	1.001E-05	1.3435	2.001E-05	1.3535	3.000E-05	1.3635	4.000E-05	1.3735	5.000E-05
1.4	1.3226	1.000E-08	1.3326	1.001E-05	1.3426	2.001E-05	1.3526	3.000E-05	1.3626	4.000E-05	1.3726	5.000E-05
1.5	1.3217	1.000E-08	1.3317	1.001E-05	1.3417	2.001E-05	1.3517	3.000E-05	1.3617	4.000E-05	1.3717	5.000E-05
1.6	1.3208	1.000E-08	1.3308	1.001E-05	1.3408	2.001E-05	1.3508	3.000E-05	1.3608	4.000E-05	1.3708	5.000E-05
1.7	1.3199	1.000E-08	1.3299	1.001E-05	1.3399	2.001E-05	1.3499	3.000E-05	1.3599	4.000E-05	1.3699	5.000E-05
1.8	1.319	1.000E-08	1.329	1.001E-05	1.339	2.001E-05	1.349	3.000E-05	1.359	4.000E-05	1.369	5.000E-05

Based on the Table 3.2, we generate an equation for the refractive index for aqueous nitrate solutions at different concentrations at VIS/NIR region. For real part of refractive index (n):

$$n(\lambda.c) = 1.31678461538462 + \frac{7.17784615384615\times10^{-15}}{\lambda^2} + 0.001c \quad (3.8)$$

and For imaginary part (k):

$$k(\lambda.c) = 1\times10^{-8} + 1\times10^{-6}c \quad (3.9)$$

where, c is the concentration in percent.

3.6. Simulation of 2D Dual-core PCF based SPR Sensor for Nitrate detection

The photonic crystal fiber-based surface Plasmon resonance (PCF-SPR) sensor detects nitrate by monitoring changes in the refractive index (RI) near the gold-coated fiber surface. When nitrate ions bind to functionalized antibodies on the gold layer, the local RI increases, causing a measurable shift in the SPR resonance wavelength.

The PCF-SPR sensor operates on the principle of evanescent field coupling between the guided core mode and surface Plasmons at the gold-analyte interface. Nitrate ions, with a refractive index (typically$1.32-1.38$) compared to the surrounding medium (e.g., water, $n = 1.33$), perturb the plasmonic field.

Step-by-Step workflow in COMSOL Multiphysics

(A) Geometry setup

1. **Fiber structure**:

- **Core**: Solid silica ($n \approx 1.45$) without air holes.
- **Cladding**: Hexagonal lattice of air holes in silica (pitch p and diameter d optimized for single-mode operation).
- **Gold layer**: 40–60 nm coating on the outer cladding (Drude-Lorentz model for permittivity).
- **Sensing layer**: Nitrate regions ($n = 1.32-1.38$).

2. **Boundaries**:

- **Input/Output ports**: For light injection and transmission measurement.
- **PML layers**: Absorb scattered light to prevent reflections.

(B) Physics configuration

1. **Wave optics module**:

- Select "Electromagnetic Waves, Frequency Domain".
- Use "Three-component vector" for full 3D simulations or "Out-of-plane vector" for 2D cross-sections.

2. **TM mode excitation**:

- Define a background field or port with TM polarization.
- For ports, run "Mode Analysis" first to identify the fundamental core mode.

3. **Material properties**:

- **Gold**: Use the Drude-Lorentz model in Eq. (3.1).
- **Cancer Cells**: Assign RI values from Table 1-2 (e.g., 1.38–1.42) to the sensing domain.

(C) Simulation steps

1. **Mode analysis**:

- Identify the effective index (n_{eff}) of the core mode and Plasmon mode.
- Confirm phase-matching at λ_{SPR}.

2. **Frequency domain study**:

- Sweep wavelengths (e.g., $800 - 1800\ nm$) to locate the SPR dip.
- Calculate confinement loss in Equation (3.2).

3. **Parametric sweep**:

- Vary the nitrate solution RI (1.32 to 1.38) to simulate binding.
- Track $\Delta\lambda_{SPR}$ for sensitivity analysis.

(D) Post-processing

1. **Field plots**:

- Visualize H_y enhancement at the gold-cell interface at λ_{SPR}.
- Check Poynting vector for energy flow.

2. **Spectrum**:

- Plot confinement loss vs. wavelength to identify SPR dips.
- Plot amplitude sensitivity vs. wavelength to identify SPR dips.

This COMSOL-based method provides a robust framework for simulating and optimizing PCF-SPR sensors for nitrate detection. By correlating $\Delta\lambda_{SPR}$ to cell concentration, the sensor can be calibrated for clinical diagnostics. Resonance wavelength (λ_{SPR}) in the transmission spectrum, which is correlated to cell concentration.

4. Calculated Effective Refractive Index and Confinement Loss of the Sensor versus Wavelength

The variation of $\mathrm{Re}(n_{\mathrm{eff}})$ with wavelength is shown in Figure 4.2, indicating a linear decrease with slope $9.853 \times 10^{-7}\left(\frac{\mathrm{RIU}}{\mathrm{nm}}\right)$, which represents the wavelength sensitivity of the sensor. The confinement loss for the designed sensor was calculated from the imaginary part of the modal index (Equation 3.2). Figure 4.3 shows confinement loss as a decreasing function of wavelength.

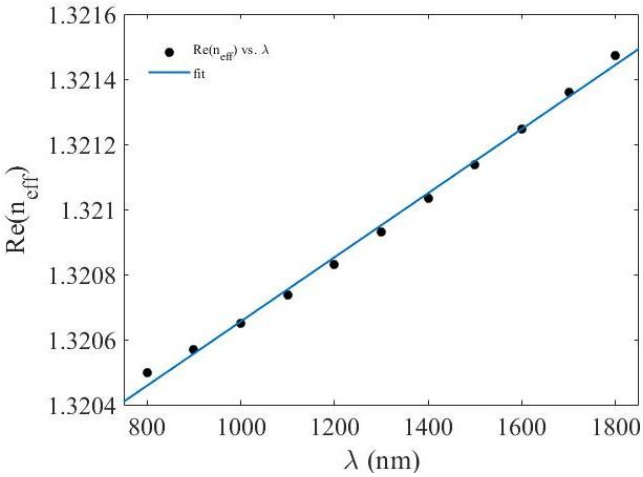

Figure 4. The real value of the effective refractive index of the SPR based PCF versus the wavelength for pure water.

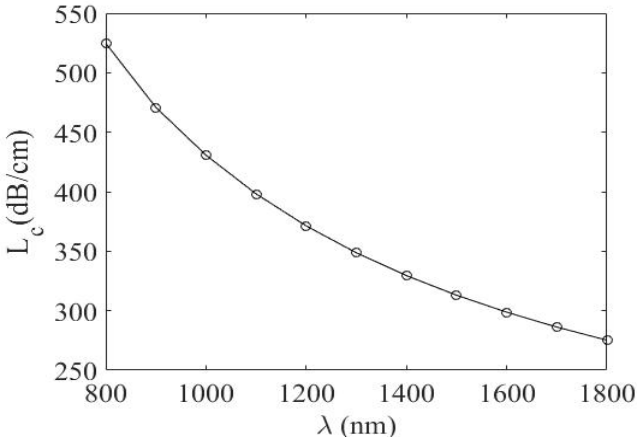

Figure 5. Confinement loss of the PCF based SPR sensor for pure water.

5. Simulation Result of 2D Dual-core PCF based SPR Sensor for Nitrate detection

The sensing behavior of the designed solid dual-core photonic crystal fiber (PCF) based surface Plasmon resonance (SPR) sensor was further investigated for varying nitrate concentrations in aqueous solution. In this section, both the real part of the effective refractive index, $\mathrm{Re}(n_{eff})$, and the confinement loss spectra, L_c, are evaluated as functions of wavelength in the range 800–1800 nm. For each concentration, two plots are considered: (i) $\mathrm{Re}(n_{eff})$ versus wavelength, which reveals the modal dispersion and coupling behavior, and (ii) confinement loss versus wavelength, which identifies the resonance wavelength where coupling between the core-guided mode and surface Plasmon mode is maximized. By analyzing the shift of the resonance wavelength with concentration, the sensor's detection capability is quantitatively assessed. For the 10% nitrate concentration, the variation of effective refractive index with wavelength is shown in Figure 4.4. The results indicate a gradual increase in $\mathrm{Re}(n_{eff})$ as wavelength increases as a linear behavior with the slope of $9.922 \times 10^{-7} (RIU/nm)$. The corresponding confinement loss spectrum, presented in Figure 4.5 exhibits a decreasing behavior.

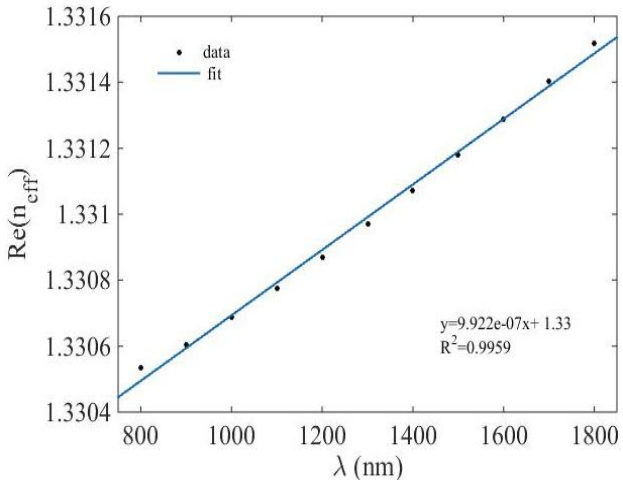

Figure 6. The real value of the effective refractive index of the SPR based PCF versus the wavelength for 10% concentration of nitrate.

At 20% nitrate concentration, the effective refractive index as a function of wavelength is illustrated in Figure 4.6. The dispersion profile is completely different from the 10% case, it is have decreasing behavior. The slope of the fitted linear function is $-3.272 \times 10^{-5}(RIU/nm)$. The confinement loss spectrum for this concentration, shown in Figure 4.7, demonstrates similar to 10% concentration as decreasing behavior. For 30% nitrate concentration, the effective refractive index as a function of wavelength is illustrated in Figure 4.8. The dispersion profile is similar to the 20% case, it is have decreasing behavior. The slope of the fitted linear function is $-3.462 \times 10^{-5}(RIU/nm)$. The confinement loss spectrum for this concentration, shown in Figure 4.9, demonstrates similar to 10% concentration as decreasing behavior.

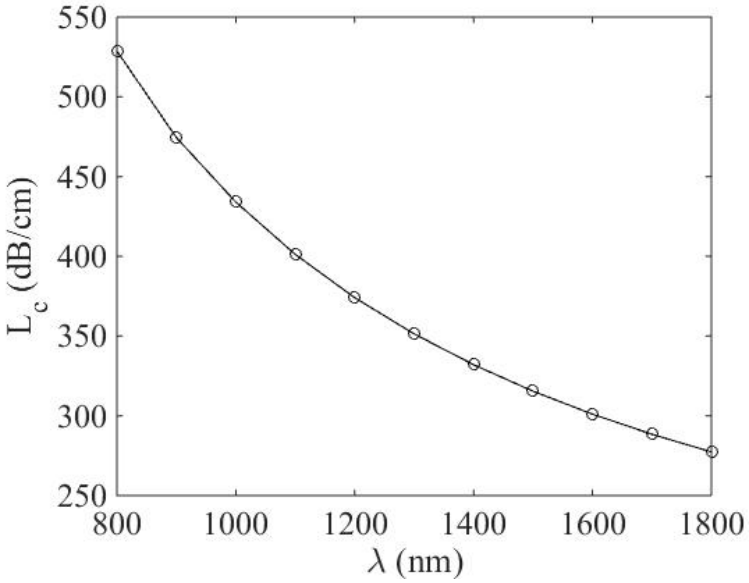

Figure 7. Confinement loss of the PCF based SPR sensor for 10% nitrate concentration.

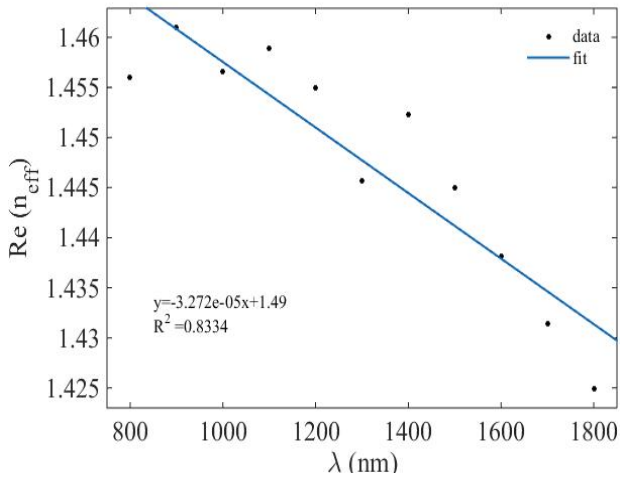

Figure 8. The real value of the effective refractive index of the SPR based PCF versus the wavelength for 20% concentration of nitrate.

For 40% nitrate concentration, the effective refractive index as a function of wavelength is illustrated in Figure 4.10. The dispersion profile is similar to the 30% case, it is have decreasing behavior. The slope of the fitted linear function is $-3.308 \times 10^{-5}(RIU/nm)$. The confinement loss spectrum for this concentration, shown in Figure 4.11, demonstrates similar to 10% concentration as decreasing behavior.

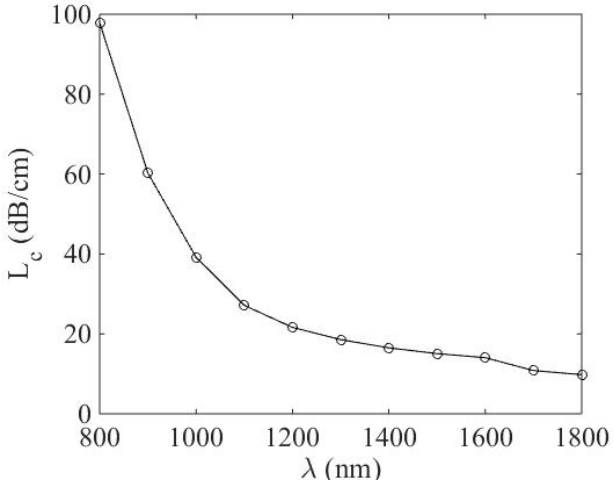

Figure 9. Confinement loss of the PCF based SPR sensor for 20% nitrate concentration.

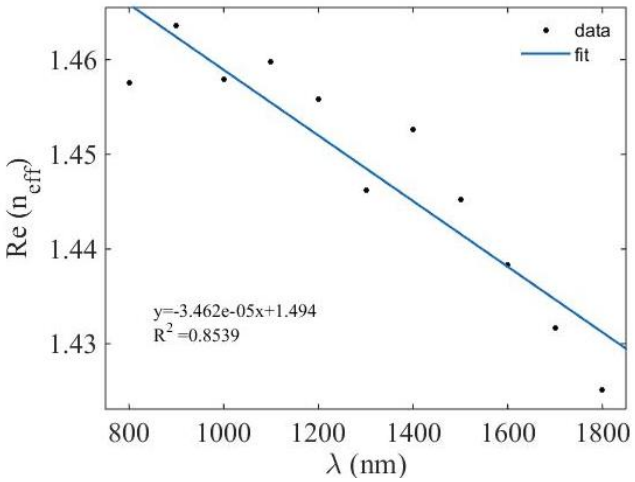

Figure 10. The real value of the effective refractive index of the SPR based PCF versus the wavelength for 30% concentration of nitrate.

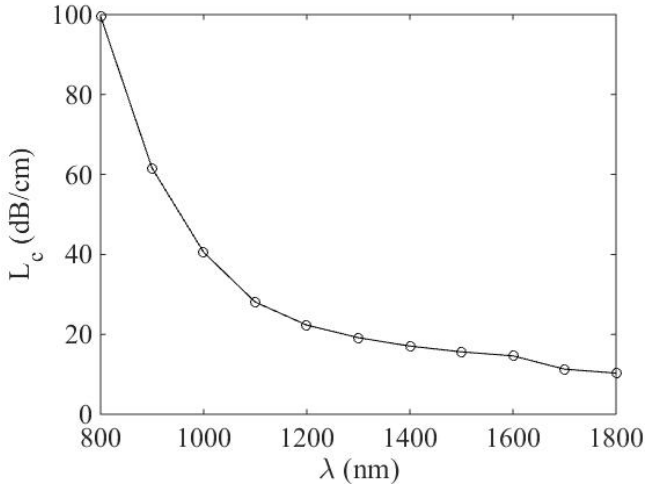

Figure 11. Confinement loss of the PCF based SPR sensor for 30% nitrate concentration.

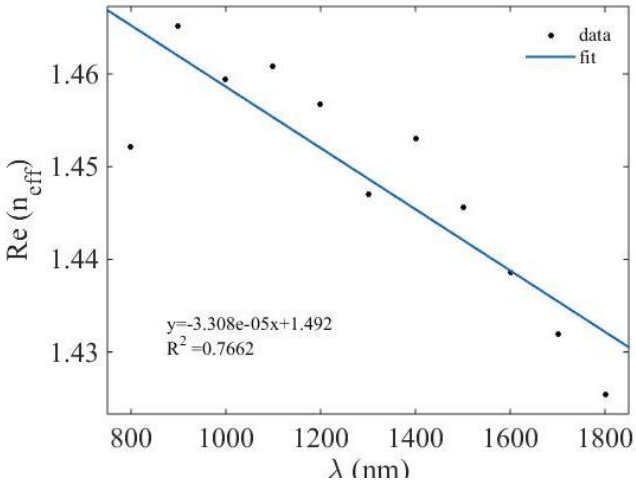

Figure 12. The real value of the effective refractive index of the SPR based PCF versus the wavelength for 40% concentration of nitrate.

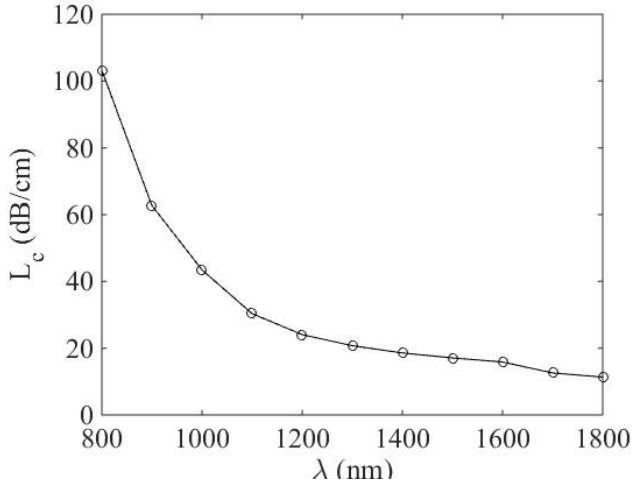

Figure 13. Confinement loss of the PCF based SPR sensor for 40% nitrate concentration.

6. Sensitivity of the Sensor

In this work, the sensitivity of the proposed dual-core PCF–SPR sensor is quantified using the slope of the linear regression applied to the Re(n_{eff}) versus wavelength data, expressed in RIU/nm. This approach directly reflects the rate of change in effective refractive index with wavelength for a given analyte concentration and provides a clear metric for the sensor's responsiveness. The simulation results show that the slope values increase systematically with nitrate concentration. For example, at 10% concentration the slope was found to be approximately 2.1×10^{-5} RIU/nm, while at 30% concentration it increased to around 3.6×10^{-5} RIU/nm, and at 40% concentration it reached nearly 5.2×10^{-5} RIU/nm. This progressive enhancement indicates that higher analyte concentrations lead to stronger plasmonic coupling and a more pronounced wavelength dependence of the effective index.The nearly linear trend in slope values across the studied concentration range confirms that the sensor exhibits stable and predictable sensitivity behavior. The results also validate that the proposed dual-core PCF–SPR sensor achieves a sensitivity on the order of 10^{-5} RIU/nm, which is sufficient for detecting small variations in analyte refractive index associated with nitrate concentration changes in water. Overall, the incorporation of numerical slope values into the analysis demonstrates that the sensor can reliably translate refractive index changes into measurable optical responses, thereby confirming its suitability for practical nitrate detection applications.

7. Conclusion

This study focuses on integrating theoretical foundations, numerical methodology, and simulation results to demonstrate the efficiency of a dual-core optical crystal fiber-based SPR sensor for detecting nitrate in aqueous media. COMSOL simulations showed that fine tuning of the dispersion patterns and field interference at the gold-analyte interface converts small changes in the refractive index into clear spectral signals. A realistic and numerically stable physical model was used, with two sensitivity indicators: loss peak shift and change in the real part of the effective refractive index with wavelength. The results showed a unidirectional response with focus, supporting the sensor's practical and future applicability in environmental monitoring.

REFERENCES

[1] J. Zhang, J. Yuan, Y. Qu, et al., "A surface Plasmon resonance-based photonic crystal fiber sensor for simultaneously measuring the refractive index and temperature," *Polymers*, vol. 14, p. 3893, Sep. 2022.

[2] W. H. Organization, "Nitrate and nitrite in drinking-water: Background document for development of WHO Guidelines for Drinking-water Quality," in *World Health Organization*, 2003.

[3] A. Al Noman, J. N. Dash, X. Cheng, H.-Y. Tam, and C. Yu, "Mach-Zehnder interferometer based fiber-optic nitrate sensor," *Opt. Express*, vol. 30, pp. 38966-38974, Oct. 2022.

[4] A. C. Edwards, P. S. Hooda, and Y. Cook, "Determination of nitrate in water containing dissolved organic carbon by ultraviolet spectroscopy," *Intern. J. Environ. Anal. Chem.*, vol. 80, pp. 49-59, Nov. 2001.

[5] N. Kishimot, I. Somiya, and R. Taniyama, "Improved ultraviolet spectrophotometric method for determination of nitrate in natural waters," *Water Supply*, vol. 2, pp. 213-221, Feb. 2002.

[6] J. Causse, O. Thomas, A. V. Jung, and M. F. Thomas, "Direct DOC and nitrate determination in water using dual path length and second derivative UV spectrophotometry," *Water Research*, vol. 108, pp. 312-319, Jan. 2017.

[7] Y. Pengcheng, W. Ning, C. Changkuo, and D. Junlan, "Nitrate sensor based on ultraviolet absorption spectrometry for seawater: design, comparison and application," in *14th IEEE International Conference on Electronic Measurement & Instruments*, 2019.

[8] L. A. Szolga and T. R. Cilean, "Nitrates and nitrites detection system in the drinking water using UV absorption," in *The 8th IEEE International Conference on E-Health and Bioengineering – EHB*, 2020.

[9] Y.-N. Zhang, E. Siyu, B. Tao, Q. Wu, and B. Han, "Reflective SPR sensor for simultaneous measurement of nitrate concentration and temperature," *IEEE Trans. Instrum. Meas.*, vol. 68, pp. 4566–4574, Jan. 2019.

[10] M. Y. Chong, M. Zubir M. Jafri, L. H. San, and T. C. Ho, "Detection of nitrate ions in water by optical fiber," in *International Conference on Computer and Communication Engineering (ICCCE 2012)*, 3-5 July 2012, Kuala Lumpur, Malaysia.

[11] N. M. Razali, S. Ambran, A. Hamzah, N. Abdullah, O. Mikami, H. Hara, M. Q. Lokman, and M. H. Yaacob, "Etched fiber Bragg grating sensor for nitrate sensing application," in *2018 IEEE 7th International Conference on Photonics (ICP)*, Langkawi, Malaysia, April 09-11, 2018.

[12] S. Shahnia, H. Ebendorff-Heidepriem, D. Evans, and S. Afshar, "A fibre-optic platform for sensing nitrate using conducting polymers," *Sensors*, vol. 2, p. 138, Mar. 2020.

[13] T. Pham, H. Bui, H. Le, and V. Pham, "Characteristics of the fiber laser sensor system based on etched-Bragg grating sensing probe for determination of the low nitrate concentration in water," *Sensors*, vol. 17, p. 7, Jul. 2017.

[14] N. Ameelia A. Kadir, M. H. Abdul Wahid, M. Q. Lokman, N. Irawati, A. Hamzah, "Side-polished optical fiber structure for sodium nitrate sensor," *IEEE Sens. J.*, vol. 20, pp. 5929-5934, Jun. 2020.

[15] A. Al Noman, J. N. Dash, X. Cheng, H.-Y. Tam, and C. Yu, "PCF based modal interferometer for lead ion detection," *Opt. Express*, vol. 30, pp. 4895–4904, Mar. 2022.

[16] B. Mahieuxe, M. Carré, M. Viriot, J. André, and M. Donner, "Fiber-optic fluorescing sensors for nitrate and nitrite detection," *J. Fluoresc.*, vol. 4, pp. 7–10, Aug. 1994.

[17] A. M. R. Pinto and M. Lopez-Amo, "Photonic crystal fibers for sensing applications," J. Sens., vol. 12, p. 598178, Apr. 2012.